J Adv Ceram

Research Article

A fast composition-stability machine learning model for screening MAX phases and guiding discovery of Ti_2SnN

Zhiyao Lu, Yun Fan, Zhaoxu Sun, Xiaodong He, Chuchu Yang, Hang Yin, Jinze Zhang, Guangping Song, Yongting Zheng, Yuelei Bai✉

Cite this article: Lu Z, Fan Y, Sun Z, et al. *J Adv Ceram* 2025, **14**(4): 9221050. https://doi.org/10.26599/JAC.2025.9221050

ABSTRACT: To explore the MAX phase with experimental value over a wider range, a data-driven machine learning (ML) model was trained to rapidly predict the stability of MAX phases via a random forest classifier (RFC), support vector machine (SVM), and gradient boosting tree (GBT), where the deemed significant descriptors were compiled from the literature and the stability of 1804 combinations of MAX phases was collected. Using this well-trained model, 190 new MAX phases were screened from 4347 MAX phases, 150 of which met the criteria for thermodynamic and intrinsic stability on the basis of first-principles calculations. Additionally, with the help of the ML model, the mean number of valence electrons and the valence electron deviation are the two most critical factors influencing stability. Additionally, one of these predicted MAX phases, Ti_2SnN, was experimentally synthesized through Lewis acid substitution reactions at 750 °C, with interesting A-site deintercalation and self-extrusion. First-principles calculations revealed that Ti_2SnN has lower elastic properties, higher damage tolerance and fracture toughness, and a higher coefficient of thermal expansion (CTE).

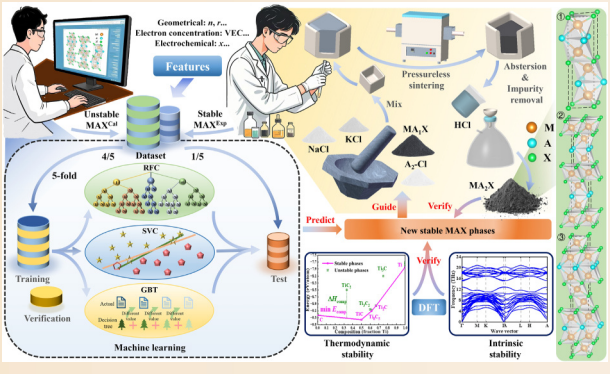

KEYWORDS: MAX phases; machine learning (ML); Ti_2SnN; first principles; self-extrusion

1 Introduction

1.1 Background of MAX phases

In the past 20 years, a class of ternary layered transition metal carbides and nitrides, referred to as MAX phases, have attracted significant attention for their potential applications in high-temperature structural and thermal protection [1–4]. Their distinctive hybrid bond type and layered structures amalgamate the advantageous traits of ceramics and metals, which include attributes such as high modulus, oxidation resistance, and radiation resistance, along with elevated electrical and thermal conductivity, exceptional thermal shock resistance, machinability, substantial fracture toughness, and remarkable damage tolerance [3,5–8]. Beyond these inherent qualities, the extensive elemental compositions of MAX phases offer analogous yet subtly distinct properties, opening up avenues for tuning their intrinsic properties for specific applications. For example, the thermal expansion coefficients of MAX phases typically vary in the range of (5–15)×10^{-6} K^{-1} [9]. In the case of a nickel-based superalloy matrix (coefficient of thermal expansion (CTE) = 16.7×10^{-6} K^{-1}) coupled with an 8YSZ ceramic top layer (CTE = 11.5×10^{-6} K^{-1}), choosing thermally matched and oxidation-resistant Cr_2AlC as a bonding layer (CTE = 12.6×10^{-6} K^{-1}) over traditional MCrAlY (CTE = (15.4–17.5)×10^{-6} K^{-1}) would offer distinct advantages [10].

The utilization of tunability within the MAX-phase family extends far beyond its aforementioned applications. In the realm of electrical contacts, various MAX phases are often selected as ohmic contact materials for different semiconductor materials to reduce the interface energy barrier, facilitating the input and output of current [11], such as Ti_3SiC_2 for 4H-SiC [12] and Ti_2AlN for GaN [13]. Moreover, suitable MAX phases can be chosen to accomplish bonding tasks effectively. For example, Ti_3SiC_2 can be utilized to bond SiC and C_f/SiC composites [14–16]. Furthermore, as the exclusive precursor to MXenes [17] showcases vast prospects in fields such as adsorption [18], Raman enhancement [19], and electrocatalysis [20], the abundance of MAX phases constrains the available options for MXenes. As a large family of two-dimensional materials, MXenes can serve as excellent adsorbents or substrate materials for various applications. For example, $Ti_2C(OH)$ demonstrates outstanding

National Key Laboratory of Science and Technology on Advanced Composites in Special Environments and Center for Composite Materials and Structures, Harbin Institute of Technology, Harbin 150080, China.

✉ Corresponding author. E-mail: baiyl@hit.edu.cn

Received: December 5, 2024; Revised: January 28, 2025; Accepted: February 20, 2025

© The Author(s) 2025. This is an open access article under the terms of the Creative Commons Attribution 4.0 International License (CC BY 4.0, http://creativecommons.org/licenses/by/4.0/).

adsorption properties for Pb^{2+} ions in wastewater [18], Nb_2C significantly enhances the Raman peak of the SARS-CoV-2 spike protein by over 10^6 times, greatly lowering the minimum detection concentration [19], and Mo_2CT_x improves the utilization efficiency of Pt nanoparticles, enhancing both the activity and stability of water electrolysis reactions [20].

1.2 Importance of ML in materials

Therefore, to achieve better tunability, it is urgent and necessary to systematically identify all MAX phases that are viable for experimental use. However, as scientific research progresses, the scope of MAX phase screening continues to broaden. For example, the discovery of Nb_2SB [21,22] in 2019 expanded the definition of MAX phases beyond ternary-layered carbides and nitrides to include ternary-layered borides. Similarly, the discovery of Mn_2GaC extended the range of transition metal elements from early transition metals to encompass the entire transition metal range [23]. Consequently, when considering only the MAX elements within the range depicted in Fig. 1 and with n limited to 1–3 (as there are no reports on the preparation of pure MAX phases with $n > 3$ [24]), the number of potential combinations has increased to 4347. This raises the question for researchers in this field of why some of them exist, and others do not. In other words, which would be next?

The theoretical methodology available at this time to answer the above question is to carry out careful *ab initio* calculations by considering their intrinsic stability and thermodynamic ability to compete with all other competing phases. The former ensures that the target phases lie around a local minimum of energy and is usually examined by their phonons. The latter means that the phases with a given composition have lower energy than all other competitive phases and their combinations, which can be effectively addressed via a linear optimization procedure proposed by Dahlqvist *et al.* [25]. Although these methodologies indeed have succeeded in identifying new MAX phases and MAB phases [24,26,27], they necessitate calculating the energy of all competing phases, resulting in a substantial workload and low efficiency. Additionally, these calculations are performed at $T = 0$ K, serving only as a reference and not reflecting the conditions of high-temperature synthesis. Moreover, the absence of competitive phases for some lesser-studied elements often leads to an underestimation of the calculated competitive enthalpy [25,28].

Recently, artificial intelligence (AI), including machine learning (ML), has achieved powerful performance in life and industry [29], especially for the analysis, design, and prediction of materials [30–34]. In particular, more efficient ML can predict high-performance materials directly by learning high-dimensional input data (descriptors) [32] rather than extracting limited information from linear combinations of different descriptors [35]. These descriptors can be derived from the properties of the atom itself, such as mass and radius, or from the calculation of density functional theory (DFT). In fact, ML has been successful in MAX phase research: Frey *et al.* [36] used a large number of data from DFT calculations to make accurate predictions about MAX phase stability, but the use of these descriptors also greatly reduces the efficiency of machine learning. In addition, although the ML method has been applied to predict the mechanical and thermal properties of different material systems [37], the DFT method still has advantages in terms of accuracy and interpretability and is highly compatible with experimental results in the MAX phase [26], perovskite [38], and other fields. Therefore, after ML is used to predict stability, the DFT method can be used to predict stability. The DFT is used to calculate the performance of the selected few stable MAX.

1.3 Objectives of the study

Therefore, in the present work, a convenient and efficient ML model was established for the stability of MAX phases on the basis of the elemental properties only, with the overall workflow illustrated in Fig. 2. Herein, data on all known stable MAX phases were collected from the experimental literature, and nonexistent MAX phases were identified via the existing first-principles results. This dataset was summarized into feature values on the basis of factors influencing compound formation, such as geometric factors and electronic concentration. Owing to their excellent predictive capabilities and flexibility [39–43] for materials, models such as the random forest classifier (RFC) [44], support vector classifier (SVC) [44], and gradient boosting tree (GBT) [45] have been employed for the present prediction of MAX phases. Although the machine learning algorithms used in this study, such

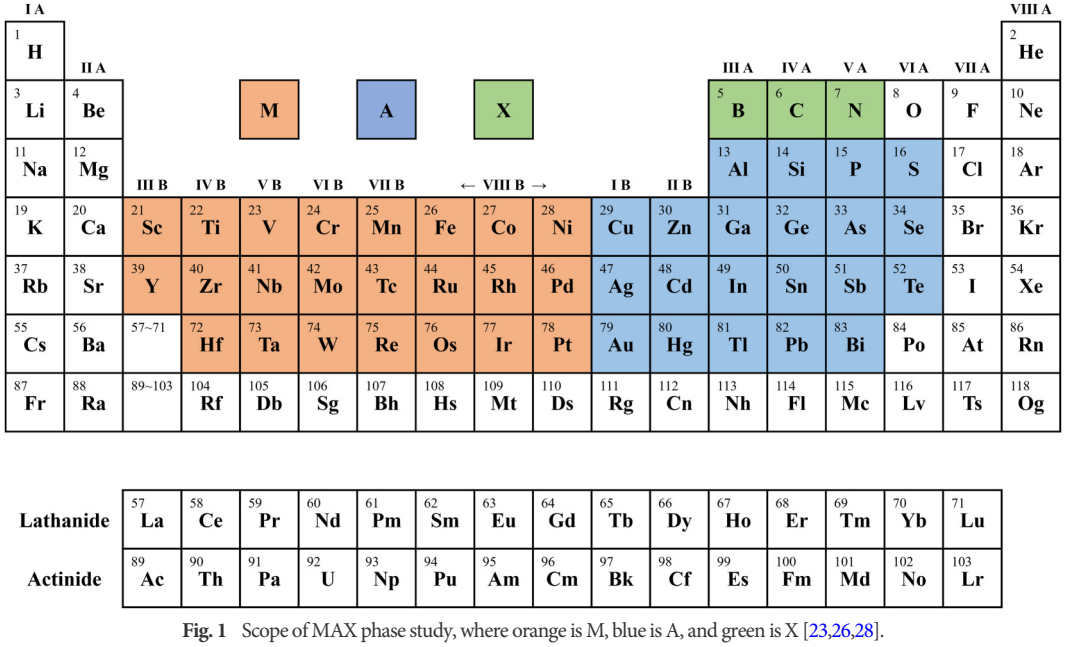

Fig. 1 Scope of MAX phase study, where orange is M, blue is A, and green is X [23,26,28].

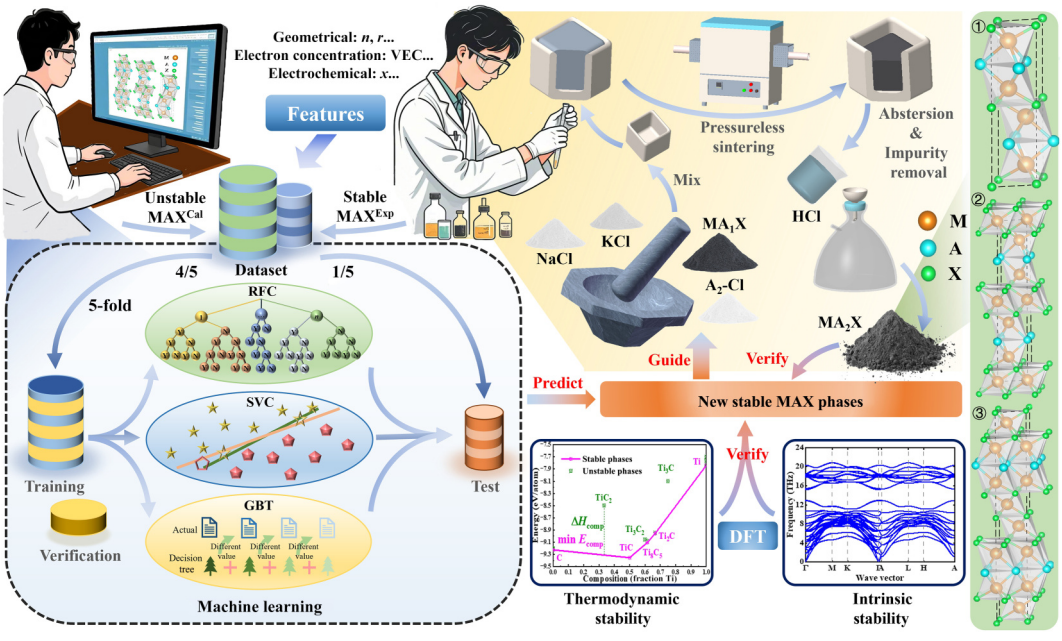

Fig. 2 Overall workflow of this paper.

as RFC, support vector machine (SVM), and GBT, are well known, our research innovatively applies them to the study of MAX phase stability. We constructed a unique dataset by integrating a large amount of experimental and computational data and carefully selected features according to the specific characteristics of MAX phases. This approach not only improves the efficiency of screening MAX phases but also provides a new perspective for the discovery of new MAX phases.

Furthermore, the predictions from the ML models successfully guided the first synthesis and characterization of Ti_2SnN, with a brief introduction to its mechanical and thermal properties. This research will contribute to a better understanding of MAX phase stability from an elemental perspective and further accelerate the future discovery of new MAX phases.

2 Computational and experimental details

2.1 Machine Learning

2.1.1 *Label of stability*

The dataset was compiled from various published studies and consists of 101 experimentally reported phases labeled "1" (feasible for experimental synthesis) [46] and 1703 phases labeled "0" (computationally unstable) [24,47,48]. The experimentally reported phases are listed in Table S1 in the Electronic Supplementary Material (ESM), with more detailed references available in the ESM. Importantly, some sources within this dataset are difficult to verify. For example, some experimental reports on MAX phases originate from articles published decades ago that do not provide X-ray diffraction (XRD) data [49], whereas others appear only as descriptions in reviews [50]. Additionally, certain MAX phases may exist only in thin films [51] or may exhibit instability at room temperature, with A-site atoms prone to extrusion [52].

All the data in these studies are considered reliable but have been distinctly labeled for differentiation in Table S1 in the ESM. The criteria for determining unstable phases are based on a competitive enthalpy (ΔH_{comp}) greater than 36 meV/atom relative to all competing phases and intrinsic instability, which is indicated by the presence of imaginary frequencies in the phonon spectrum. The threshold for determining thermodynamic stability is set at 36 meV/atom because instances such as Nb_2SB and Nb_2SC exhibit competitive enthalpies greater than zero [47]. This discrepancy may be related to differences between the competitive enthalpies at actual synthesis temperatures and those calculated at 0 K, thus necessitating a broader criterion for stability assessment. Furthermore, the competitive enthalpy may be underestimated due to the potential absence of competing phases. In other words, the competitive enthalpy for unstable phases can only be underestimated, thereby confirming their inherent instability.

2.1.2 *Selection of features*

In the selection of features, to represent the combination of elements with MAX phases, data on the valence electron concentration (VEC), atomic radius (r) [53], electronegativity (x), mass (m), and average atomic energy (E) of each element are collected in the present work. The average atomic energy solely originates from Vienna *ab initio* simulation package (VASP) calculations of the most stable structures of individual elements. Notably, the p–d interaction between atoms at the M and X sites is remarkably strong within the MAX phases, leading to highly covalent M–X bonds. Conversely, for M–A bonding, the interaction between the M-d electrons and the A-p electrons is weaker than that between the M and X atoms. The A-d electrons seem to play no role in bonding. Hence, for M and X atoms, the total number of valence electrons, including the d electrons in the valence band, termed VEC, is utilized. However, for A atoms, the average number of roaming electrons (itinerant electrons (IE)) [46] per atom is chosen for representation, but for convenience, they are all labeled VEC in this paper. All the data used are also listed in Table S2 in the ESM.

In addition, the electronic concentration and geometric factors significantly influence the formation of compounds [46]. Regarding the electronic concentration, Barsoum [9] suggested that the formability of MAX phases can be analyzed from the perspective of the average number of valence electrons per unit cell volume (n_{val}). Since the cell volume must be obtained through structural optimization via first-principles calculations, in past studies, it was found to have a strong correlation with the

elemental radii [47]. Thus, n_{val} can use the average valence electron concentration ($\overline{VEC}$) together with the radius of each element as an alternative. Additionally, deviations in the valence electron concentration (S_{VEC}) were taken into account Eqs. (1) and (2):

$$\overline{VEC} = \frac{\sum n_i VEC_i}{\sum n_i} \tag{1}$$

$$S_{VEC} = \sqrt{\sum \frac{n_i}{N}\left(1 - \frac{VEC_i}{\overline{VEC}}\right)^2} \tag{2}$$

where i represents the atoms at different sites, n_i represents the number of atoms at different sites, VEC_i represents the valence electron concentration of atoms at different sites, and N represents the total number of atoms in this structure.

The MAX phase can be considered the insertion of A atoms into MX, resulting in the replacement of the X element on the M atom side with the A element [50]. As geometric factors, both the following S_r and S_{r^*} represent the amount of lattice distortion caused by inserting an A atom into an MX crystal (Eqs. (3) and (4)):

$$S_r = \sqrt{\frac{1}{2}\left(1 - \frac{A_r}{\bar{r}}\right)^2 + \frac{1}{2}\left(1 - \frac{X_r}{\bar{r}}\right)^2} \tag{3}$$

$$S_{r_*} = \sqrt{\frac{1}{2}\left(1 - \frac{A_r + M_r}{\overline{r_*}}\right)^2 + \frac{1}{2}\left(1 - \frac{X_r + M_r}{\overline{r_*}}\right)^2} \tag{4}$$

where $\bar{r} = (A_r + X_r)/2$, representing the average atomic radius of elements A and X, $\overline{r_*} = (A_r + X_r)/2 + M_r$, representing the average bond length considering their respective bonds to elements M. M_r, A_r, and X_r are the radii of the M, A, and X atoms, respectively.

Moreover, previous work [48] indicated that MAX phases are likely stable only when the difference in electronegativity (Δx) exceeds 1.5. Although this trend does not hold true for Mo_2GaC, it remains a singular exception. Therefore, this factor is also considered one of the characteristic values, as expressed in Eq. (5):

$$\Delta x = \frac{|M_x - A_x - X_x|}{M_x} \tag{5}$$

where M_x, A_x, and X_x represent the electronegativity of the M, A, and X atoms, respectively. As a result, the following 21 features are listed for each MAX phase: layer number (n), M valence electron concentration (M_{VEC}), M_r, M_x, M atomic mass (M_m), M atomic energy (M_E), A valence electron concentration (A_{VEC}), A_r, A_x, A atomic mass (A_m), A atomic energy (A_E), X valence electron concentration (X_{VEC}), X_r, X_x, X atomic mass (X_m), X atomic energy (X_E), $\overline{VEC}$, Δx, S_{VEC}, S_r, and S_{r^*}.

2.1.3 *Training setting*

After the chemical formula information of the collected samples is read with Python, features are generated and used as inputs for the RFC, SVC, and GBT models. Both the RFC and GBT methods exhibit strong robustness to noise, effectively addressing noise issues that may arise from factors such as aging, as observed in materials such as Ti_2TlC. Moreover, the SVC method is particularly efficient in handling high-dimensional data, which is why these approaches were selected for use together. All the data were randomly divided into a training set (4/5) and a test set (1/5). Then, k-fold cross-validation [54] is adopted to ensure the repeatability of the results: The training set is randomly divided into five parts, where each one is successively used as a verification set, with the test results averaged for hyperparameter adjustment. Notably, the hyperparameters are traversed through the loop for better results. These trained ML models were then used to predict the experimental preparation possibility of the MAX phases in all permutations.

The Pearson correlation coefficient ($\rho_{X,Y}$) was used to determine whether each feature was closely related to each other [43]. If one is highly correlated with another, it is a duplicate feature and can be removed, which ensures that each feature is as unique as possible. In the present work, the Pearson correlation coefficient of two features, X and Y ($\rho_{X,Y}$) can be expressed as Eq. (6):

$$\rho_{X,Y} = \frac{\sum (X_i - \overline{X})(Y_i - \overline{Y})}{\sqrt{\sum (X_i - \overline{X})^2 (Y_i - \overline{Y})^2}} \tag{6}$$

where X_i and Y_i represent the ith values of an array of two different input features and $\overline{X}$ and $\overline{Y}$ represent the expected values of the two input features.

To assess the contribution of each feature to the model's prediction, the Shapley additive explanations (SHAP) [32] model was employed. SHAP is based on Shapley values, which explain the model's decision-making process by calculating the contribution of each feature to the prediction of a single sample. These values are derived from cooperative game theory and, when applied to model interpretation, measure the marginal contribution of each feature to the prediction outcome. To quantify the global impact of features on the overall model, we used the mean absolute SHAP value. This metric calculates the average contribution of a feature across all samples, effectively neutralizing the influence of both positive and negative contributions. This provides a comprehensive measure of the feature's importance. For feature ii, we calculate the absolute SHAP values for all samples N in the dataset and then take the average. The specific calculation formula is as Eq. (7):

$$\begin{aligned}\text{Mean}\,(|\text{SHAP value}|) &= \frac{1}{N}\sum_{j=1}^{N}\left|\phi_{ii}(j)\right| \\ &= \frac{1}{N}\sum_{j=1}^{N}\left|f(S\cup\{ii\}) - f(S)\right|\end{aligned} \tag{7}$$

where $\phi_{ii}(j)$ is the SHAP value for feature ii in the jth sample, N is the total number of samples, $f(S)$ is the model's prediction using only the features in subset S, and $f(S\cup\{ii\})$ is the model's prediction with the addition of feature ii.

2.2 First principles

First-principle calculations were carried out via VASP [55], which is based on DFT. The Perdew–Burke–Ernzerhof (PBE) functional, a form of generalized gradient approximation (GGA) [56], was utilized for exchange-correlation energy. Ion–electron interactions were managed through the projector-augmented wave method [57], with a consistent cutoff energy of 550 eV. The Gamma mesh of k-point sampling, adjusted according to the cell size, consistently ensured total energy convergence within ±1 meV/atom. Geometry optimizations were pursued with rigorous convergence values, aiming for total energy convergence within $\pm 10^{-8}$ eV/cell and atomic forces below 10^{-7} eV/Å. The conjugate-gradient method [58] facilitates atomic relaxation during optimization.

Stability criteria primarily encompass thermodynamic stability and intrinsic stability. The former relies on the "linear

programming method" developed by Dahlqvist [25], which involves determining the most stable combination of competing phases with a given elemental composition (lowest energy) and comparing the energy difference with that of a targeted compound. If the energy of the compound is lower, it is deemed thermodynamically stable with the negative ΔH_{comp} (Eq. (8)):

$$\Delta H_{comp} = E - E_{comp}\left(b^{M}, b^{A}, b^{X}\right) = E - \min\left(\sum_{i}^{n} x_i E_i\right) \quad (8)$$

where E and E_i are the average atomic energy of the target and competition phases, respectively, while b^M, b^A, and b^X are the respective ratios of M, A, and X, respectively. x_i and E_i are the amount of compound i and its energy, respectively. Importantly, the lowest energy that all competing phases can compose at that ratio, which is E_{comp}, should be minimized under restrictive conditions (Eq. (9)):

$$\begin{cases} x_i \geq 0, \sum_{i}^{n} x_i = 1 \\ \sum_{i}^{n} x_i b_i^{M} = b_M, \sum_{i}^{n} x_i b_i^{A} = b_A, \sum_{i}^{n} x_i b_i^{X} = b_X, \\ b_M + b_A + b_X = 1 \end{cases} \quad (9)$$

where b_i^M is the ratio of the number of M atoms in compound i, with a similar case for b_i^A and b_i^X.

Intrinsic stability refers to the Gibbs free energy of a structure being at or near a local minimum for small deformations. In practice, this can be determined by examining the lattice dynamics (phonons): Stable structures should not have any negative vibrational frequencies, indicating that they are at a local energy minimum. For phonon calculations, the "frozen phonon method" is employed with the help of Phonopy code [58], where small displacements are applied on atoms around their equilibrium positions, with the resulting energy for the dynamical matrix and vibrational frequencies. Here, a fixed finite displacement amplitude of 0.01 Å is applied in a 3 × 3 × 1 supercell to calculate the Hellmann–Feynman forces [58]. In these DFT simulations, tolerances are set to ensure convergence of the total energy within $\pm 10^{-8}$ eV/cell. For 211 phases with space groups $P6_3/mmc$, A_{1g}, E_{1g}, and E_{2g} have Raman activity [59].

The elastic stiffness matrix (c_{ij}) was determined by fitting stress–strain curves, where a series of strains were applied with the resulting stress. In particular, the stiffness matrix was derived from the stress corresponding to the strain applied up to a maximum strain amplitude of ±0.030 Å with a step size of 0.015 Å, which involves calculating the second derivatives of the energy with respect to the atomic displacements. Here, the convergence criteria were set at a total energy within $\pm 10^{-6}$ eV per cell and Hellmann–Fynman forces less than 1 meV/Å. From c_{ij}, the bulk modulus (B) and shear modulus (G) were first calculated via the Voigt and Reuss approximations, with their average via the Hill approximation [60]. The Young's modulus (E) and Poisson's ratio (μ) were subsequently calculated as Eqs. (10) and (11):

$$E = \frac{9BG}{3B + G} \quad (10)$$

$$\mu = \frac{1}{2} \times \frac{3B - 2G}{3B + G} \quad (11)$$

The deformation resistance of chemical bonds under hydrostatic pressure (P) can be used to characterize the bond strength quantitatively. After the relative bond length (d/d_0) is fitted as a function of P with a quadratic polynomial, the slope is $1/k$, where k is defined as the bond stiffness (Eq. (12)) [61,62]:

$$k = \left|\frac{\mathrm{d}\left(d/d_0\right)}{\mathrm{d}P}\right|^{-1} = \left|\frac{\mathrm{d}\left(C_0 + C_1 P + C_2 P^2\right)}{\mathrm{d}P}\right|^{-1} = \left|C_1 + 2C_2 P\right|^{-1} \quad (12)$$

where d_0 is the bond length at 0 GPa, and C_i (i = 0, 1, and 2) represents the quadratic fitting coefficient.

The codes of VASP and Phonopy are used to perform quasiharmonic approximation (QHA) calculations, in which the free energy $F(V,T)$ (V is the volume and T is the temperature) is expressed as the sum of three contributions (Eq. (13)):

$$F(V,T) = E_{tot}(V) + F_{qha}(V,T) + F_{el}(V,T) \quad (13)$$

where $E_{tot}(V)$ is the total energy at T = 0 K, which is directly calculated via VASP; $F_{qha}(V,T)$ is the free energy due to atomic vibrations (phonon); $F_{el}(V,T)$ is the finite-temperature free energy due to electronic excitation. The second term $F_{qha}(V,T)$ is given by Eq. (14):

$$F_{qha}(V,T) = \sum_{i}\left(\frac{1}{2}\hbar\omega_i + k_B T \ln\left(1 - \mathrm{e}^{-\frac{\hbar\omega_i}{k_B T}}\right)\right) \quad (14)$$

where ω_i is the phonon frequency, $\hbar$ is the reduced Planck constant, and k_B is the Boltzmann constant. Finally, $F_{el}(V,T)$ is expressed by Eq. (15):

$$F_{el}(V,T) = E_{el}(V,T) - TS_{el}(V,T) \quad (15)$$

where E_{el} represents the electronic energy of the system, which accounts for the energy due to the electrons at a given volume and temperature. S_{el} is the entropy associated with the system. Once all contributions to the free energy are available, the equilibrium volume $V_{eq}(T)$ and corresponding $F(V,T)$ at each temperature (T) can be determined by minimizing the free energy as a function of V at this temperature. It follows that the temperature dependence of ($V_{eq}(T)$) and heat capacity ($c_p(T)$) can be determined from Eq. (16):

$$\left.\frac{\partial F(V,T)}{\partial V}\right|_{V_{eq}(T)} = 0, c_p = -T\left.\frac{\partial^2 (V,T)}{\partial T^2}\right|_{V_{eq}(T)} \quad (16)$$

Furthermore, the linear thermal expansion ($\Delta l/l_0$) can be calculated via Eq. (17), where V_{300K} represents the volume of the cell at 300 K.

$$\Delta l / l_0 = \left(V(T)/V_{300K}\right)^{1/3} - 1 \quad (17)$$

2.3 Synthesis and characterizations of Ti_2SnN

Ti_2SnN was prepared by reacting the traditional MAX precursor Ti_2AlN (Laizhou Kaikai Ceramic Materials Co., Ltd., China) with the Lewis acid $SnCl_2$ (Tianjin Zhonglian Chemical Reagent Co., Ltd., China). Ti_2AlN, $SnCl_2$, NaCl, and KCl (Sinopharm Chemical Reagent Co., Ltd., China) were mixed at an atomic ratio of 1 : 1.5 : 2 : 2 and sintered under an argon atmosphere without pressure at 750 °C for 5 h in a tube furnace (GSL-1700X, Hefei Kejing Material Technology Co., Ltd., China). The product was subsequently washed with 5% HCl for 4 h to remove the residual Sn and collected again.

The XRD measurements were conducted via a Panalytical X'PERT diffractometer (PANalytical B.V., the Netherlands) equipped with a Cu Kα radiation source, with a scanning range from 5° to 90° and scanning rate of 2 (°)/min. Additionally,

Raman spectroscopy was employed for supplementary phase composition via an Raman spectrometer (inVia-Reflex, Renishaw, UK) with a wavelength of 532 nm, a light intensity of 10%, and a duration of 2 min. The microstructures were observed via a scanning electron microscope (SEM; Merlin Compact, Carl Zeiss AG, Germany) equipped with an energy-dispersive spectroscopy (EDS) system and a transmission electron microscope (TEM; Talos-F200X-G2, Thermo Fisher Scientific, USA) equipped with an EDS system.

3 Results and discussion

3.1 Stable phase screening based on ML search and DFT verification

To select the most meaningful features, the Pearson correlation coefficient was first calculated on the basis of the dataset, as shown in Fig. S1 in the ESM. After removing the features with high correlation (> 0.7), only the following features are retained: n, M_m, M_E, A_{VEC}, A_x, A_E, X_m, X_E, $\overline{VEC}$, Δx, S_{VEC}, and S_{r^*}. The corresponding correlation matrix heatmaps are shown in Fig. 3. All training data are also provided in Table S3 in the ESM.

In the training process, a grid search is employed to identify the hyperparameter combination that yields the highest accuracy. For RFC models, we analyze the depth of the decision trees and the number of trees to enhance performance. While the number of trees affects the model's complexity and predictive capability, limiting the depth of the trees helps prevent overfitting and improves generalizability. In SVC model, the kernel function and penalty coefficient are optimized. The penalty coefficient controls the model's tolerance for misclassification errors, whereas the kernel function determines how data are mapped in high-dimensional space. Similarly, the depth and number of trees are also examined in GBT model.

As illustrated in Figs. 4(a), 4(c), and 4(e), all three models achieve high verification accuracy on the validation set. The RFC model achieved the highest accuracy of 0.9861 with the following hyperparameters: 62 trees (n_estimators = 62), a maximum depth of 18 (max_depth = 18), a minimum of 1 sample per leaf (min_samples_leaf = 1), and a minimum of 2 samples to split an internal node (min_samples_split = 2). The SVC model reached a maximum accuracy of 0.9778 with a penalty coefficient of 10 (C = 10), a radial basis function kernel (Kernel = 'rbf'), and a gamma value of 0.1. The GBT model achieved a peak accuracy of 0.9806 with 85 trees (n_estimators = 85), a maximum depth of 5 (max_depth = 5), and a learning rate of 0.1. As shown in the test set in Figs. 4(b), 4(d), and 4(f), the performance of the models can be evaluated in terms of accuracy, precision, and recall on the test set. For the RFC, the accuracy was 0.978, the precision was 1.00, and the recall was 0.556. The SVC achieved an accuracy of 0.964, a precision of 0.677, and a recall of 0.556. Finally, the GBT obtained an accuracy of 0.978, a precision of 0.857, and a recall of 0.677. The trained RFC and GBT have the same high accuracy, while the RFC model has a higher precision rate in predicting the stable phases, with a higher recall rate for the GBT model.

The trained RFC, SVC, and GBT models were subsequently used to examine the stability of the other MAX phases (more information can also be obtained from Table S4 in the ESM). The stable phases predicted by the three models are listed in Tables S5–S7 in the ESM, where those identified experimentally, those predicted by the ML model, and experimental preparation phases that were not predicted are marked in black, red, and green, respectively. Thermodynamic stability was first used to verify the predicted phases (Table 1). The competitive enthalpy data for the MAX carbides and nitrides with A-sites in the Al and Si columns are from Ref. [48], whereas the remaining data are calculated in the present work, with the competitive phases and competitive enthalpies in Table S8 in the ESM. According to the RFC model, 115 new phases were predicted, whereas 12 failed to pass the thermodynamic stability criterion. The corresponding values are

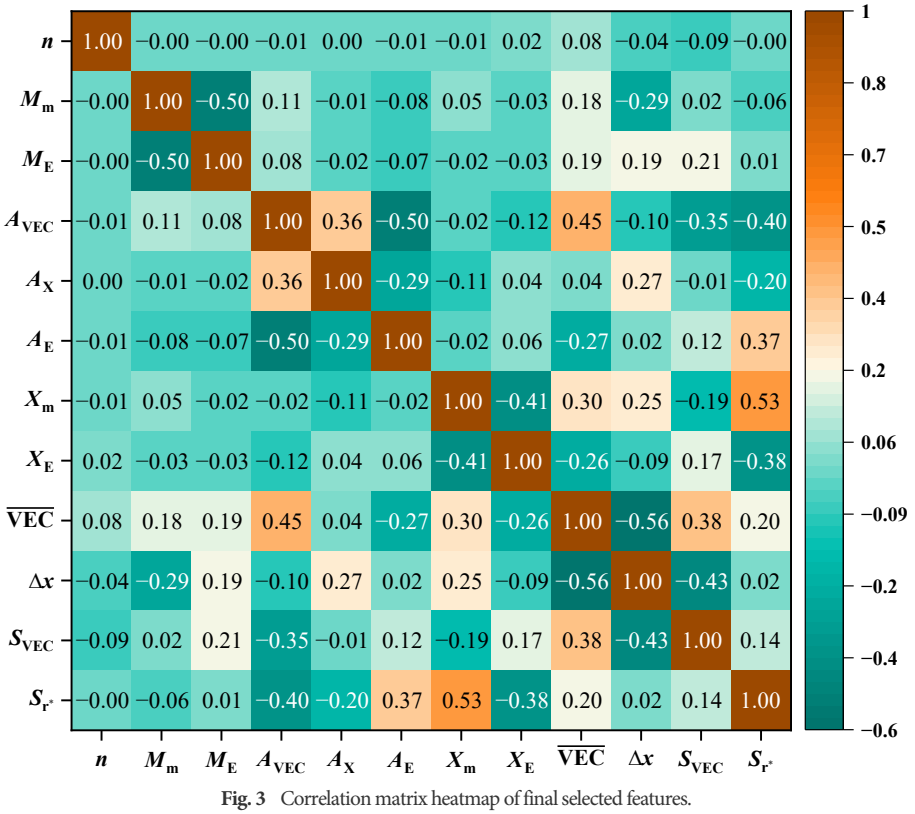

Fig. 3 Correlation matrix heatmap of final selected features.

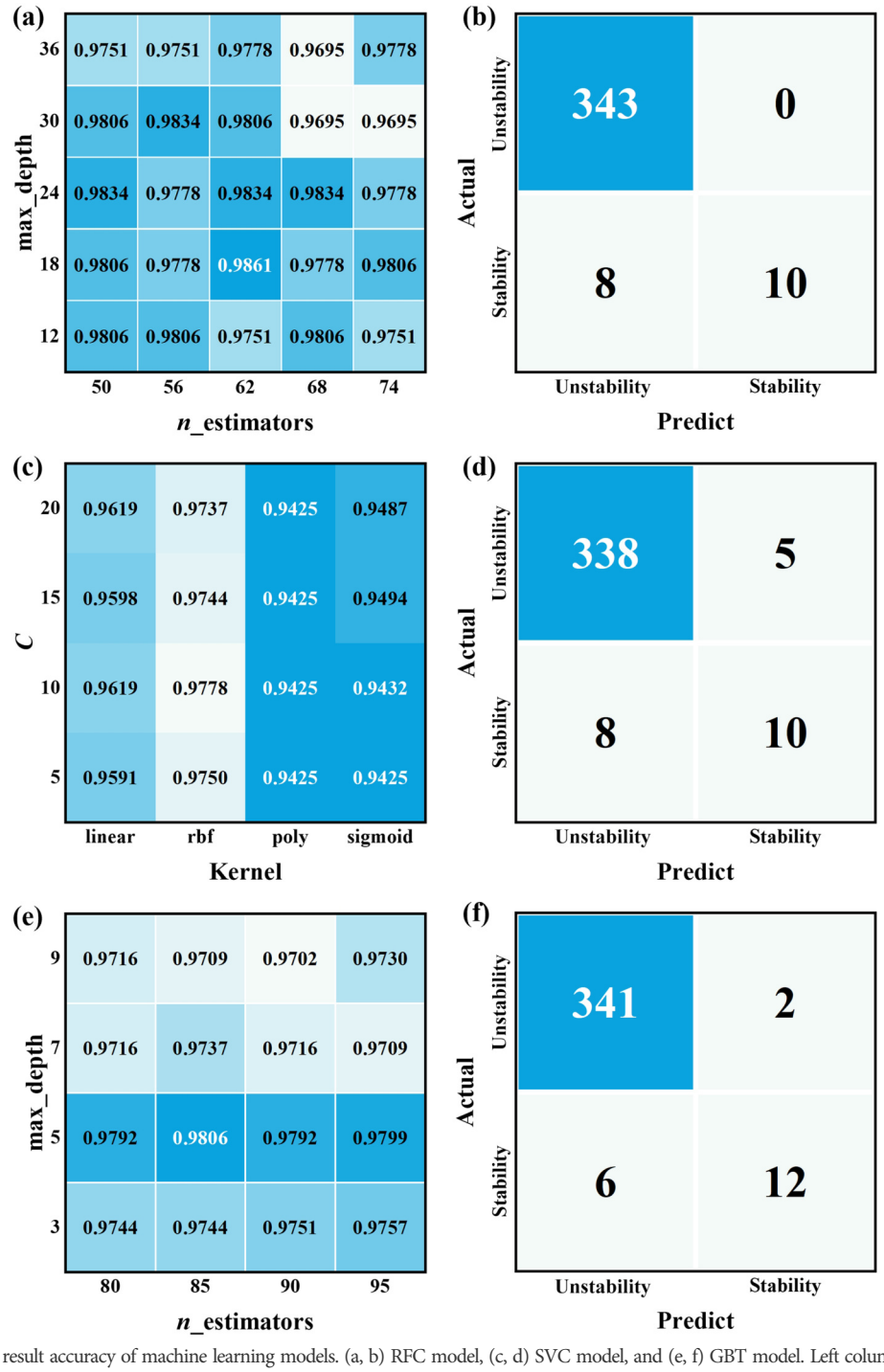

Fig. 4 Grid search and result accuracy of machine learning models. (a, b) RFC model, (c, d) SVC model, and (e, f) GBT model. Left column is average accuracy of validation set of five-fold cross method, and right column is confusion matrix when trained model predicts test set.

127 and 22 according to the SVC model and 165 and 32 according to the GBT model. In all the cases, the absence of imaginary phonon frequencies (Fig. S2 in the ESM) further indicates their intrinsic stability. As a result, a total of 150 MAX phases (Fig. S3 in the ESM) met the criteria of both thermodynamic and intrinsic stability but were not synthesized, leading to significantly improved screening efficiency. For all these predicted new phases, it is worth noting that the lower the competitive enthalpy is, the easier it will be to prepare.

Figure 5(a) visualizes the importance of features on the basis of their average absolute SHAP values (|SHAP|), where larger |SHAP| values indicate greater impact on the stability of MAX phases. Clearly, $\overline{VEC}$ and S_{VEC} are crucial factors influencing the formation ability of MAX phases. Plotting all MAX phases into nonstable, computationally stable, and experimentally stable categories on the basis of these two parameters yields Fig. 5(b). Except for phases such as Ti_2AuN and Mn_2GaC, which were reported in thin-film form [23,63], all stable phases lie within the three triangular-like regions, as marked by the blue lines. Notably, these stable phases have $\overline{VEC}$ between 3.25 and 5. Each triangular-like region has a width of 0.75 and a height of approximately 0.3, whereas the vertical coordinates of the other points are approximately 0.1. The lower boundary of these triangular-like regions is determined by the integer nature of the valence

Table 1 MAX stable phase predicted by different models, where ΔH_{comp} (meV/atom) is listed in parentheses

Cu		Ag		Au	
Ti_4CuN_3	Nb_2CuC	$Ti_4AgC_3(-1)$	~~$Nb_2AgC(139)$~~	$Ti_2AuC(16)$	$Ti_4AuN_3(-11)$
				Ti_3AuC_2	Cr_2AuC
				$Ti_4AuC_3(-3)$	Nb_2AuC
				Ti_2AuN	Mo_2AuC
				$Ti_3AuN_2(6)$	

Zn		Cd		Hg	
Ti_2ZnC	V_2ZnC	Ti_2CdC	$Ti_3CdN_2(-9)$	$Ti_2HgC(-85)$	$Ti_2HgN(-29)$
Ti_3ZnC_2	$Zr_3ZnC_2(18)$	$Ti_3CdC_2(-37)$	$Ti_4CdN_3(-12)$	$Ti_3HgC_2(-72)$	$Ti_3HgN_2(-17)$
$Ti_4ZnC_3(-2)$	Nb_2ZnC	$Ti_4CdC_3(-29)$	$Nb_2CdC(34)$	$Ti_4HgC_3(-55)$	$Ti_4HgN_3(-14)$
Ti_2ZnN	$Hf_3ZnC_2(-16)$	$Ti_2CdN(-11)$			
$Ti_3ZnN_2(-1)$	$Hf_4ZnC_3(-14)$				
$Ti_4ZnN_3(-12)$					

Al		Ga		In		Tl	
Ti_2AlC	Zr_2AlC	Sc_2GaC	$Zr_2GaC(13)$	Sc_2InC	Zr_3InC_2	$Sc_2TlC(8)$	$Zr_4TlC_3(4)$
Ti_3AlC_2	Zr_3AlC_2	Ti_2GaC	$Zr_3GaC_2(-12)$	$Sc_2InN(26)$	$Zr_4InC_3(2)$	Ti_2TlC	Zr_2TlN
$Ti_4AlC_3(0)$	$Zr_4AlC_3(-1)$	Ti_3GaC_2	$Zr_4GaC_3(-1)$	Ti_2InC	Zr_2InN	$Ti_3TlC_2(-16)$	$Zr_3TlN_2(27)$
Ti_2AlN	$Zr_2AlN(-19)$	Ti_4GaC_3	$Zr_2GaN(10)$	Ti_3InC_2	$Zr_3InN_2(23)$	$Ti_4TlC_3(9)$	~~$Nb_2TlC(62)$~~
$Ti_3AlN_2(13)$	Nb_2AlC	Ti_2GaN	Nb_2GaC	$Ti_4InC_3(2)$	Nb_2InC	$Ti_2TlN(18)$	Hf_2TlC
Ti_4AlN_3	Nb_4AlC_3	$Ti_3GaN_2(17)$	$Nb_3GaC_2(1)$	Ti_2InN	Hf_2InC	$Ti_3TlN_2(32)$	$Hf_3TlC_2(-15)$
V_2AlC	Hf_2AlC	$Ti_4GaN_3(-20)$	$Nb_4GaC_3(-14)$	$Ti_3InN_2(6)$	Hf_3InC_2	$Ti_4TlN_3(8)$	$Hf_4TlC_3(3)$
V_3AlC_2	Hf_3AlC_2	V_2GaC	Mo_2GaC	$Ti_4InN_3(-15)$	$Hf_4InC_3(1)$	~~$V_2TlC(140)$~~	$Hf_2TlN(9)$
V_4AlC_3	$Hf_4AlC_3(-8)$	$V_3GaC_2(2)$	$Hf_2GaC(-1)$	$V_2InC(-4)$	$Hf_2InN(-62)$	~~$Zr_2TlB(39)$~~	
V_2AlN	$Hf_2AlN(4)$	$V_4GaC_3(3)$	$Hf_3GaC_2(-14)$	~~$Zr_2InB(116)$~~		Zr_2TlC	
Cr_2AlC	Ta_2AlC	V_2GaN	$Hf_4GaC_3(-1)$	Zr_2InC		$Zr_3TlC_2(-16)$	
	Ta_3AlC_2	Cr_2GaC	$Hf_2GaN(-6)$				
	Ta_4AlC_3	Cr_2GaN	Ta_2GaC				
		Mn_2GaC	$Ta_3GaC_2(-5)$				
		~~$Zr_2GaB(269)$~~	Ta_4GaC_3				

Si		Ge		Sn		Pb	
$Ti_2SiC(17)$	$V_2SiC(11)$	Ti_2GeC	$Zr_4GeC_3(-2)$	Sc_2SnC	$Zr_4SnC_3(2)$	Sc_2PbC	$Zr_3PbC_2(-17)$
Ti_3SiC_2	$Nb_2SiC(23)$	Ti_3GeC_2	~~$Nb_2GeB(91)$~~	Ti_2SnC	$Zr_2SnN(16)$	Ti_2PbC	$Zr_4PbC_3(4)$
Ti_4SiC_3		Ti_4GeC_3	Nb_2GeC	Ti_3SnC_2	Nb_2SnB	$Ti_3PbC_2(-11)$	$Zr_2PbN(4)$
		$Ti_2GeN(-29)$	$Nb_3GeC_2(17)$	$Ti_4SnC_3(2)$	Nb_2SnC	$Ti_4PbC_3(13)$	Hf_2PbC
		V_2GeC	$Hf_2GeC(8)$	$Ti_2SnN(-38)$	Hf_2SnC	~~$V_2PbC(180)$~~	$Hf_3PbC_2(-17)$
		$V_3GeC_2(27)$	$Hf_3GeC_2(-11)$	V_2SnC	Hf_3SnC_2	$Zr_2PbB(12)$	$Hf_4PbC_3(5)$
		Cr_2GeC	$Hf_4GeC_3(-3)$	~~$Zr_2SnB(145)$~~	$Hf_4SnC_3(1)$	Zr_2PbC	
		Zr_2GeC	$Ta_2GeC(-10)$	Zr_2SnC	Hf_2SnN		
		$Zr_3GeC_2(-6)$	$Ta_3GeC_2(33)$	Zr_3SnC_2	~~$Ta_4SnC_3(67)$~~		

P		As		Sb		Bi	
$Ti_2PC(2)$	~~$Nb_2PB(44)$~~	$Ti_2AsC(-21)$	$Nb_2AsB(24)$	$Sc_2SbC(-52)$	$Zr_4SbC_3(-24)$	$Sc_2BiC(-98)$	$Zr_4BiC_3(-41)$
$Ti_3PC_2(-9)$	Nb_2PC	$Ti_3AsC_2(-28)$	Nb_2AsC	~~$Ti_2SbB(159)$~~	~~$Nb_2SbB(67)$~~	$Ti_2BiC(-18)$	~~$Nb_2BiB(122)$~~
$Ti_4PC_3(-6)$	~~$Nb_3PC_2(48)$~~	$Ti_4AsC_3(-19)$	~~$Nb_3AsC_2(56)$~~	$Ti_2SbC(-18)$	Nb_2SbC	$Ti_3BiC_2(-8)$	~~$Nb_2BiC(146)$~~
V_2PC	$Nb_4PC_3(18)$	V_2AsC	$Nb_4AsC_3(24)$	Ti_3SbC_2	~~$Nb_3SbC_2(97)$~~	$Ti_4BiC_3(6)$	$Hf_2BiB(-78)$
~~$V_3PC_2(58)$~~	$Hf_2PC(12)$	~~$V_3AsC_2(44)$~~	$Hf_2AsC(-2)$	$Ti_4SbC_3(3)$	~~$Nb_4SbC_3(82)$~~	~~$V_2BiC(231)$~~	$Hf_2BiC(-75)$
~~$V_4PC_3(54)$~~	$Hf_3PC_2(-8)$	~~$V_4AsC_3(60)$~~	$Hf_3AsC_2(-20)$	~~$V_2SbC(71)$~~	~~$Hf_2SbB(40)$~~	$Zr_2BiB(-32)$	$Hf_3BiC_2(-65)$
~~$Zr_2PB(213)$~~	$Hf_4PC_3(-8)$	~~$Zr_2AsB(178)$~~	$Hf_4AsC_3(-16)$	~~$V_3SbC_2(120)$~~	$Hf_2SbC(-11)$	$Zr_2BiC(-81)$	$Hf_4BiC_3(-43)$
$Zr_2PC(29)$	$Ta_2PC(11)$	$Zr_2AsC(11)$	$Ta_2AsC(-20)$	~~$V_4SbC_3(143)$~~	$Hf_3SbC_2(-24)$	$Zr_3BiC_2(-66)$	~~$Ta_2BiC(355)$~~
$Zr_3PC_2(5)$	~~$Ta_3PC_2(45)$~~	$Zr_3AsC_2(-8)$	~~$Ta_3AsC_2(41)$~~	~~$Zr_2SbB(121)$~~	$Hf_4SbC_3(-15)$		
$Zr_4PC_3(3)$	$Ta_4PC_3(15)$	$Zr_4AsC_3(-5)$	$Ta_4AsC_3(8)$	$Zr_2SbC(-29)$	~~$Ta_2SbC(161)$~~		
				$Zr_3SbC_2(-35)$	~~$Ta_3SbC_2(155)$~~		

S		Se		Te	
Ti_2SC	Nb_2SB	~~$Sc_2SeN(41)$~~	Zr_2SeB	~~$Sc_2TeN(186)$~~	$Zr_2TeC(-43)$
$Ti_3SC_2(1)$	Nb_2SC	~~$Ti_2SeB(83)$~~	Zr_2SeC	$Ti_2TeC(22)$	$Zr_3TeC_2(-18)$
$V_2SC(33)$	Hf_2SB	$Ti_2SeC(-98)$	$Zr_3SeC_2(-2)$	~~$Ti_2TeC_2(41)$~~	~~$Zr_2TeN(131)$~~
Zr_2SB	Hf_2SC	$Ti_3SeC_2(-58)$	~~$Nb_2SeB(42)$~~	~~$Ti_4TeC_3(53)$~~	~~$Nb_2TeB(122)$~~
Zr_2SC		$Ti_4SeC_3(-28)$	~~$Nb_2SeC(67)$~~	~~$Ti_2TeN(157)$~~	~~$Nb_2TeC(150)$~~
		$Ti_2SeN(34)$	Hf_2SeB	~~$V_2TeC(186)$~~	Hf_2TeB
		~~$V_2SeC(86)$~~	Hf_2SeC	~~$V_2TeN(103)$~~	$Hf_2TeC(-23)$
		$Y_2SeN(28)$		$Zr_2TeB(31)$	

Note: MAX0 discovered by experiment; MAX1 predicted only by RFC; MAX2 predicted only by SVC; MAX3 predicted only by GBT; MAX4 predicted by RFC and SVC; MAX5 predicted by RFC and GBT; MAX6 predicted by SVC and GBT; MAX7 predicted by RFC, SVC, and GBT.

electrons when calculating $\overline{VEC}$ and S_{VEC}. This also further indicates that $\overline{VEC}$ deviates from an integer value, and a smaller area for the S_{VEC} is required to form a stable phase. Figure 5(c) lists the specific stable phases represented by the pentagrams, where they are more likely to form at the edges and center (±0.25, 0.2) of the triangular regions.

3.2 Synthesis of Ti_2SnN

On the basis of the competitive enthalpy ranking (Fig. S3 in the ESM) and compatibility with our experimental conditions, Ti_2SnN was selected for experimental validation. All MAX phases containing Zr, Hf, Sc, Se, and Hg were not considered because of their low boiling points or stability problems in air. In the present

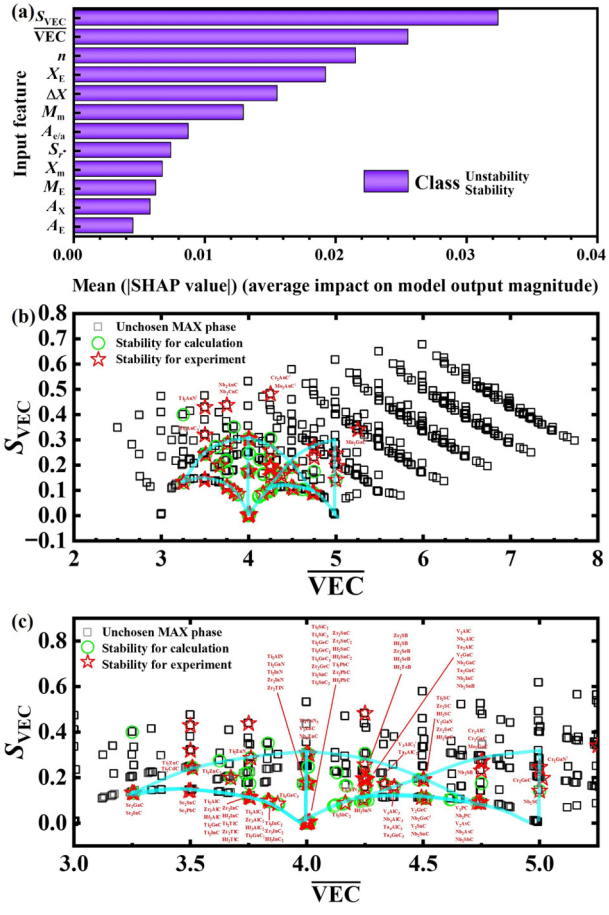

Fig. 5 (a) Feature visualization through SHAP values: Importance of each feature in MAX's SHAP model. (b) Effects of $\overline{VEC}$ and S_{VEC} on formation of MAX phase, with key regions highlighted and important MAX phases annotated in (c).

work, Ti_2AlN was chosen as the precursor for isostructural substitution instead of using elements such as Ti and Sn for traditional bottom-up synthesis to avoid the high thermodynamic barriers required for the formation of twinning in the MX sublayer. The reaction for this isostructural substitution method can be expressed as Eq. (18):

$$Ti_2AlN + 1.5SnCl_2 = Ti_2SnN + 0.5Sn + AlCl_3 \uparrow \quad (18)$$

The XRD patterns of each phase during the reaction process, along with the theoretical patterns of Ti_2AlN and Ti_2SnN, are shown in Fig. 6(a). Due to the use of isostructural substitution, the impurity tin is inevitably present after the reaction. Further treatment with 5% HCl for 4 h, as indicated by the red and blue lines in Fig. 6(a), resulted in good agreement between the experimental and computational simulations in terms of peak positions and intensities, confirming the successful synthesis of Ti_2SnN. The refinement of the XRD pattern (Fig. 6(c); Profile R-factor (R_p) = 6.79%, Weighted profile R-factor (R_{wp}) = 10.42%, and Chi-square statistic χ^2 = 14.33) shows that the experimental lattice parameters (a = 3.12468 Å and c = 13.6324 Å) match well with the calculated ones (a = 3.175 Å and c = 13.487 Å). More detailed calculations and observations of the reflection, 2θ, d-spacing, and intensities of Ti_2SnN can be found in Table S9 in the ESM. In addition, Table 2 lists the data of three similar MAX phases, e.g., Ti_2AlN [64], Ti_2InN, and Ti_2SnC [65–67]. Compared with that of Ti_2SnC, the lattice constant (a) is less affected by the change in X-position elements, whereas the lattice constant (c) of ternary carbides is greater than that of nitrides. Notably, Ti_2SnN has the largest lattice constant (a) and the smallest lattice constant (c) in comparison with Ti_2AlN and Ti_2InN. z_{Ti} refers to the position of the Ti atom on the c-axis of the cell.

Considering the similarity of the peak positions (002) and (103) of Ti_2SnN to those of Ti_2AlN, more characterization methods have been used to prove the existence of Ti_2SnN. Figure 6(b) shows that the three peaks of Ti_2AlN are located at 148, 228, and 352 cm^{-1} [64]. Conversely, the calculated frequencies of Ti_2SnN are 66, 210, 211, and 298 cm^{-1}. However, it is worth noting that the peak at 66 cm^{-1} approaches the detection limit of Raman spectroscopy and may be challenging to distinguish accurately. Although a small peak is observed at this frequency in comparison to that of Ti_2AlN, precise determination of its location remains difficult. The measured Raman peaks for Ti_2SnN are determined to be at 213 and 323 cm^{-1}, with an error margin below 8%. Specifically, the peak at 213 cm^{-1} corresponds to antisymmetric vibrations along both the a-axis and b-axis involving titanium atoms, whereas the peak at 323 cm^{-1} corresponds to antisymmetric vibrations along the c-axis.

Figure 7(a) shows the SEM image of Ti_2SnN only after Lewis acid etching. Like Ti_2SnC [68] and Cr_2GaN [52], whiskers grow out from the MAX phases, and the EDS analysis (Fig. S4 in the ESM) confirms that they are primarily composed of Sn, whereas the concentrations of Ti and N are extremely low. They tend to undergo deintercalation and self-extrusion at both room and high temperatures. More evidence of Sn growth is shown in Figs. S5(a) and S5(b) in the ESM, where many whiskers of varying diameters grow from the bulk, with quite different morphologies from those of the MAX phase prepared via the Lewis acid etching method [69]. These characteristics of deintercalation and self-extrusion also lead to problems such as poor crystal crystallinity, small and wide Raman peaks, and some differences between the calculated and experimental lattice constants. Figures 7(b) and 7(c) present SEM images of pure Ti_2SnN, revealing a distinct layered structure of MAX phases [70,71]. The EDS results, highlighted within the orange box in Fig. 7(c), further indicate that the atomic percentages of Ti, Sn, N, Al, and Pt were 47.76%, 20.63%, 29.40%, 1.63%, and 0.58%, respectively. Considering N is a light element, its EDS content data are for reference only. The low Al content compared with that of Sn and Ti suggests complete etching, again confirming the successful synthesis of Ti_2SnN. Notably, the atomic ratio of Ti to Sn slightly exceeds 2 : 1, which is consistent with the above-described self-extruding of Sn, which has been washed with HCl. However, this HCl-washed Ti_2SnN did not show whisker formation again after seven days of placement (Figs. S5(c) and S5(d) in the ESM).

Figure 7(d) depicts a single crystal of Ti_2SnN, in which Area#1 contains 42.89% and 16.83% Ti and Sn, respectively. N is a light element with a large content error (Fig. 7(i)), while the atomic ratio of Ti and Sn is approximately 2 : 1, and they are evenly distributed in the block region (Figs. 7(g) and 7(h)). Figure 7(e) presents selected area electron diffraction (SAED) for this region, with the lattice spacing along three directions at 3.78, 3.72, and 3.76 nm^{-1}. These correspond to the (101), (1$\bar{1}$0), and (0$\bar{1}\bar{1}$) planes with lattice spacings of 2.65 Å (refined calculation: 2.654 Å), 2.69 Å (refined calculation: 2.706 Å), and 2.66 Å (refined calculation: 2.654 Å) (calculated by Eq. (19), where a and c is the lattice constant, h, k, l is the Miller indices, and d_{hkl} is the crystal face spacing of the corresponding crystal face), which are consistent with the observed distances in the high-resolution image (Fig. 7(f)). The corresponding angles to these three crystal planes are 60.59°, 60.92°, and 58.49°, which are also in good agreement with the calculated angles (60.63°, 60.63°, and 58.74°, calculated via Eq. (20), where θ represents the angle between the crystal plane

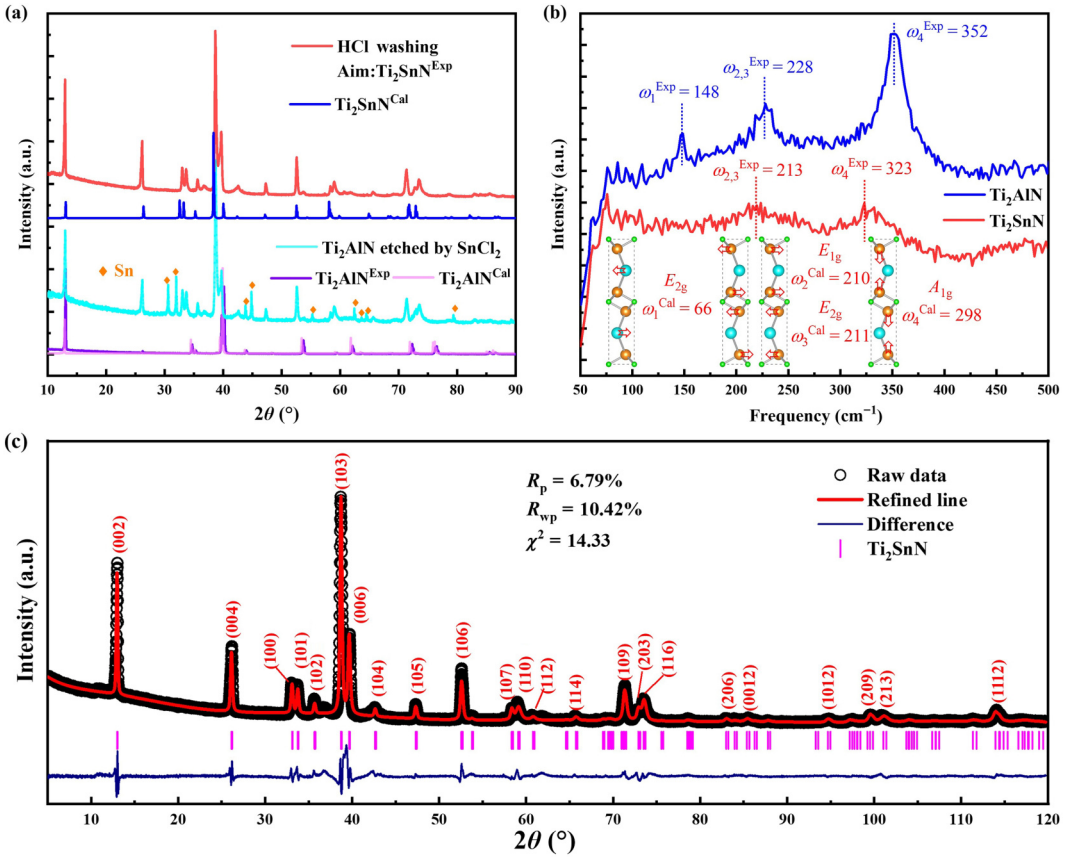

Fig. 6 (a) Experimental XRD patterns of each phase of reaction process and theoretical phases of Ti_2AlN and Ti_2SnN. (b) Raman patterns of Ti_2AlN and Ti_2SnN, and (c) XRD refinement results of Ti_2SnN.

Table 2 Lattice parameters of Ti_2SnN and three similar MAX phases: Ti_2AlN, Ti_2InN, and Ti_2SnC

Phase	a (Å)	c (Å)	V (Å^3)	z_{Ti}
Ti_2SnN^{Exp}	3.12468	13.6324	115.269	0.0789
Ti_2SnN^{Cal}	3.175 (+2%)	13.487 (−1%)	117.747 (+2%)	0.0773 (−2%)
Ti_2AlN^{Exp} [65]	2.987	13.622	105.254	—
Ti_2AlN^{Cal}	2.993 (+0.2%)	13.657 (+0.3%)	105.950 (+0.7%)	0.0855
Ti_2InN^{Exp} [66]	3.074	13.975	114.364	—
Ti_2InN^{Cal}	3.084 (+0.3%)	14.111 (+1%)	116.256 (+2%)	0.0793
Ti_2SnC^{Exp} [67]	3.164	13.69	118.7	—
Ti_2SnC^{Cal}	3.173 (+0.3%)	13.813 (+0.9%)	120.437 (+1%)	0.0805

$(h_1k_1l_1)$ and the crystal plane ($h_2k_2l_2$)). These data together indicate that the crystal axis is the $[11\bar{1}]$ direction of Ti_2SnN.

$$d_{hkl} = \frac{a}{\sqrt{\frac{4}{3}(h^2+hk+k^2)+\left(\frac{a}{c}\right)^2 l^2}} \tag{19}$$

$$\cos\theta = \frac{h_1h_2 + k_1k_2 + \frac{1}{2}(h_1k_2+h_2k_1) + \frac{3a^2}{4c^2}l_1l_2}{\sqrt{\left(h_1^2+k_1^2+h_1k_1+\frac{3a^2}{4c^2}l_1^2\right)\left(h_2^2+k_2^2+h_2k_2+\frac{3a^2}{4c^2}l_2^2\right)}} \tag{20}$$

3.3 Prediction of mechanical and thermal properties of Ti_2SnN by DFT

As a newly discovered Ti_2SnN, it is necessary to predict its fundamental properties for potential engineering applications. Here, DFT simulations were performed on Ti_2SnN to understand its fundamental mechanical and thermal properties, as detailed in Table 3. The experimentally reported Ti_2AlN, Ti_2InN, and Ti_2SnC samples were also computed to compare their performances, and their experimental data (error within 10%) are presented to verify the accuracy of the calculations in this paper.

The engineering elastic moduli of Ti_2SnN are predominantly within the lower range of MAX phase materials [9] (B: 131–261 GPa, G: 80–153 GPa, and E: 208–365 GPa). Its B (133 GPa) is similar to that of Ti_2SnC, whereas G (78 GPa) and E (196 GPa) are comparable to those of Ti_2InN and Ti_2SnC and lower than the currently reported minimum (G = 80 GPa and E = 208 GPa for Cr_2GeC [9]). In addition, Ti_2SnN has a higher Poisson's ratio (0.255) than most MAX phases do (0.15–0.24) [9]. A higher Poisson's ratio indicates that Ti_2SnN undergoes more lateral deformation under stress, which is consistent with its good

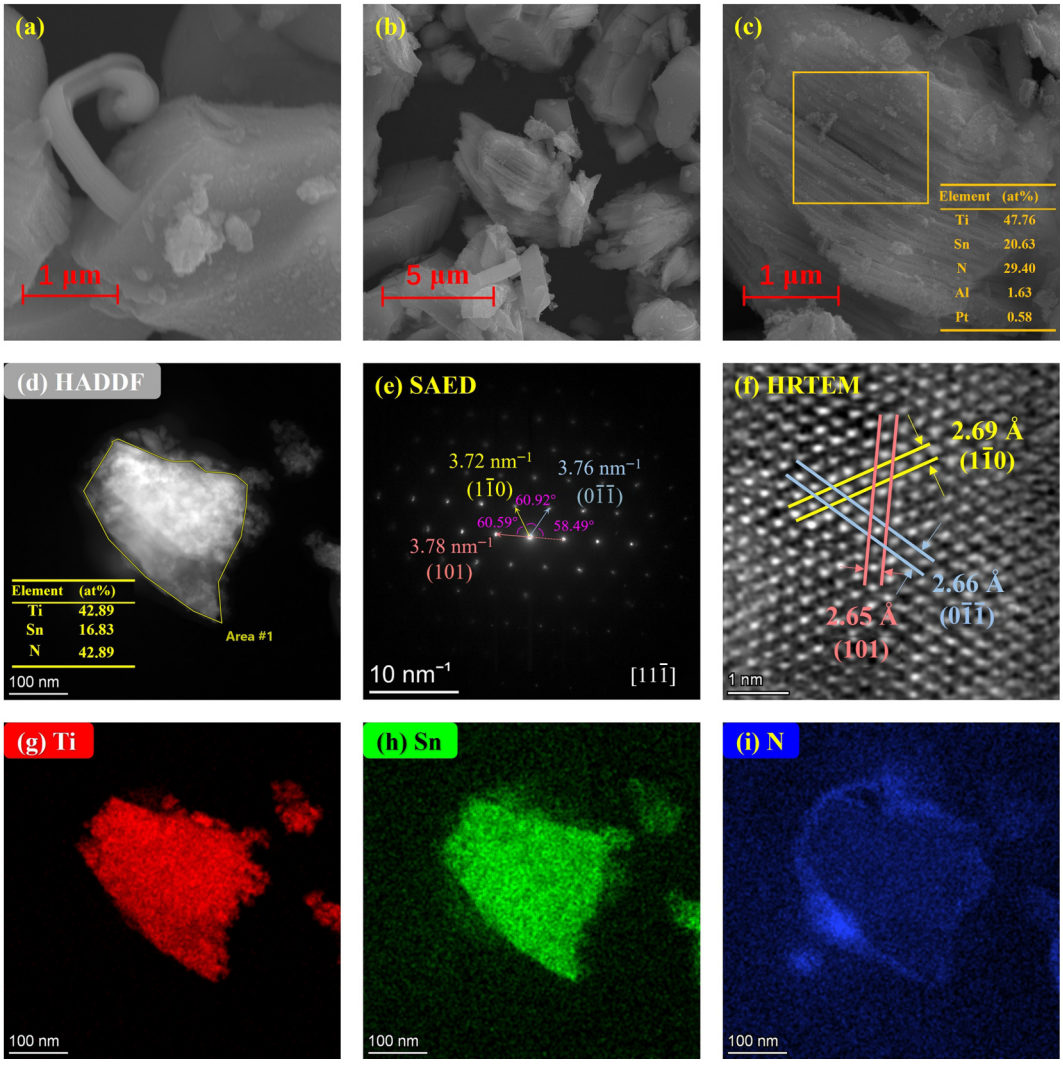

Fig. 7 (a) SEM image of Ti_2SnN/Sn before HCl washing, (b, c) SEM images of pure Ti_2SnN and its proportion of elements obtained via EDS, (d) HADDF image, (e) SAED pattern along [11$\bar{1}$], (f) HRTEM image, and (g–i) EDS images of Ti_2SnN.

ductility and lower stiffness. This characteristic enhances its ability to absorb deformation, potentially improving its impact resistance.

In addition, the bulk modulus (B_0) and its derivative (B_0'), can be estimated by fitting the effect of P on the unit cell volume via the Birch-Murnaghan equation (equation of state (EOS)) (Eq. (21)) [79]:

$$P(V) = \frac{3B_0}{2}\left[\left(\frac{V}{V_0}\right)^{-7/3} - \left(\frac{V}{V_0}\right)^{-5/3}\right] \times\left\{1 + \frac{3}{4}(B_0' - 4)\left[\left(\frac{V}{V_0}\right)^{-2/3} - 1\right]\right\} \quad (21)$$

where V is the volume of the cell, and V_0 is the volume at 0 pressure. By fitting Eq. (18), the B_0 and B_0' values of Ti_2SnN are determined to be 129 GPa and 4.42 (Fig. 8(a)), which are consistent with their c_{ij} values (133 GPa). Figure 8(a) also illustrates the variation in the normalized lattice constants (a/a_0 and c/c_0) with increasing pressure, and a gradual decrease in the curve slope indicates greater compression resistance due to decreasing bond lengths. The smaller compression along the c-axis suggests greater deformation resistance in that direction, which is consistent with $c_{33} > c_{11}$.

A further quantitative characterization of the bond strength of MAX phases was conducted by using the "bond stiffness" model [1]. A least-square fitting of the second-order polynomial (Fig. 8(b)) on the bond length as a function of P was performed to estimate the bond stiffness (Eq. (12)). The Ti-Sn bonds exhibit the weakest bond stiffness (380 GPa), whereas the Ti-N bonds display exceptionally strong deformation resistance of 901 GPa, which is significantly greater than that of the Ti-X bonds in the other three phases (~750 GPa). Previous studies [47] have indicated that MAX and MAB phases with k_{min}/k_{max} ratios greater than 1/2, such as Ti_2SC, have low damage tolerance and brittle fracture behavior, characteristic of typical brittle indentation cracks [80]. Conversely, when the ratio is less than 1/2, the materials exhibit greater damage tolerance, with no cracks observed along the indentation diagonals [26]. Additionally, their fracture toughness typically decreases as the ratio of k_{min}/k_{max} increases [26]. It follows that the low k_{min}/k_{max} of Ti_2SnN (0.422) suggests its superior toughness, which is in line with typical MAX phases [61] but contrasts notably with that of Ti_2AlN (fracture toughness at 3.8–5.2 MPa·m$^{1/2}$ [77]).

Figure 8(c) shows the total state density and partial density of states (TDOS & PDOS) of Ti_2SnN. Like all MAX [81], there is a finite DOS value (6.629 states/eV) around the Fermi level contributed by Ti-d and Sn-p, indicating that it is an electronic conductor. The hybrid states corresponding to the Ti–Sn bond

Table 3 Calculated second-order elastic constants (c_{ij}, GPa), B (GPa), G (GPa), E (GPa), μ, B_0 (GPa), and B_0' via BM equation; weakest bond stiffness (k_{min}, GPa); strongest bond stiffness (k_{max}, GPa); ratio of bond stiffness (k_{min}/k_{max}); density of states at the Fermi level ($N(E_f)$; states·eV^{-1}·unit cell^{-1}); fitting parameters of the specific heat capacityA_{c_p} (J·g^{-1}·K^{-1}), B_{c_p} (J·g^{-1}·K^{-2}), and C_{c_p} (J·K·g^{-1}); and average linear thermal expansion coefficient (α, 10^{-6} K^{-1}) for 300–1500 K of Ti_2SnN with similar MAX phases and experimental values

	Ti_2SnN	Ti_2AlN	Ti_2AlN^{Exp}	Ti_2InN	Ti_2InN^{Cal}	Ti_2SnC	Ti_2SnC^{Exp}
c_{11}	235	305	—	239	247 [72]	259	—
c_{12}	90	72	—	56	66 [72]	75	—
c_{13}	75	83	—	99	92 [72]	67	—
c_{33}	248	305	—	232	242 [72]	264	—
c_{44}	80	126	—	93	95 [72]	93	—
c_{66}	73	117	—	92	90 [72]	92	—
B	133	154	169 [73]	135	137 [72]	133	136 [74]
G	78	119	124 [75]	85	89 [72]	94	84 [76]
E	196	284	286 [75]	210	217 [72]	228	207 [76]
μ	0.2550	0.1940	—	0.2400	0.236 [72]	0.2150	0.24 [76]
B_0	129	160	169 [73]	146	137 [72]	141	136 [74]
B_0'	4.4200	3.6200	3.5 [73]	3.9400	4.410 [72]	3.8200	3.90 [67]
k_{min}	380	439	—	422	—	406	—
k_{max}	901	775	—	719	—	704	—
k_{min}/k_{max}	0.4220	0.5660	Brittle [77]	0.5860	—	0.5770	—
$N(E_f)$	6.6290	4.3710	—	5.8710	—	3.9760	—
A_{c_p}	0.4196	0.6914	—	0.4296	—	0.4309	—
B_{c_p}	32.5419	66.4250	—	29.9292	—	29.4992	—
C_{c_p}	4.7051	10.8206	—	5.4544	—	6.6877	—
α	10.0640	11.0300, 10.9500 (~1400 K)	10.00 [78] (~1400 K)	10.3020	—	11.0200 10.6100 (~1000 K)	10.3 [74] (~1000 K)

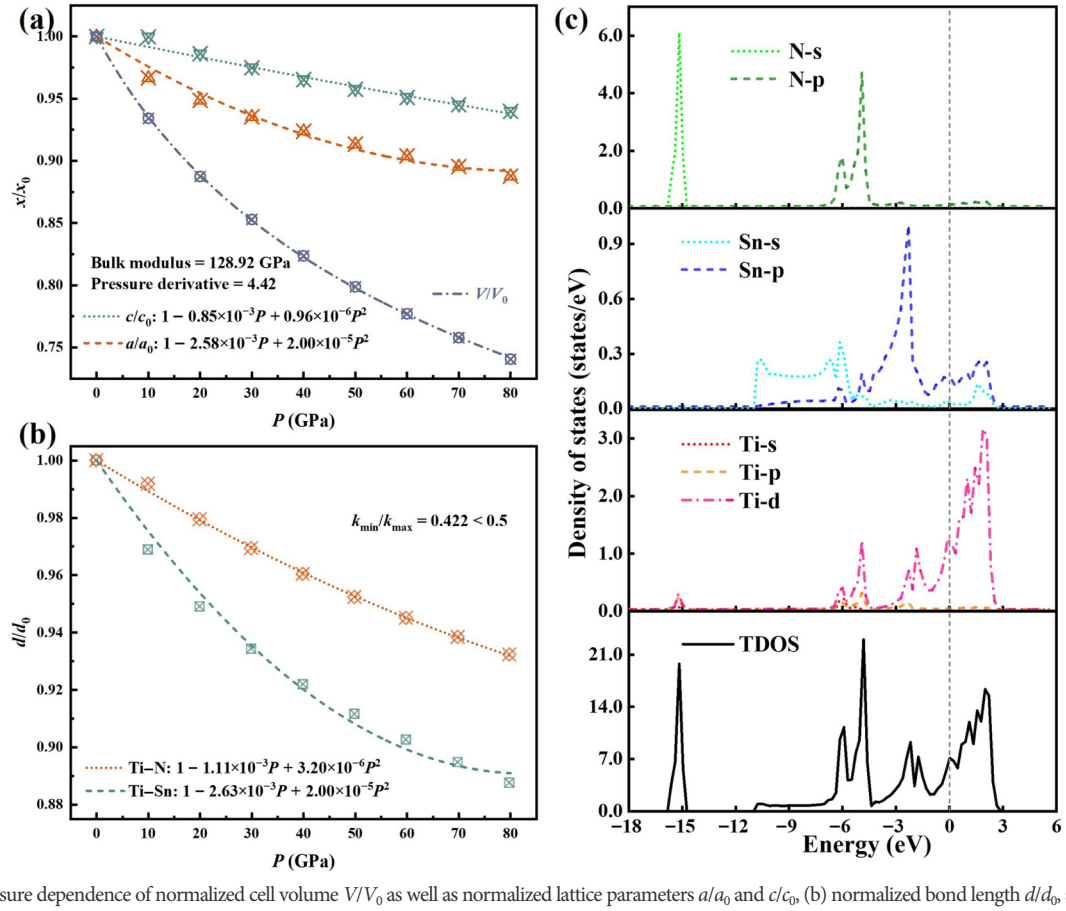

Fig. 8 (a) Pressure dependence of normalized cell volume V/V_0 as well as normalized lattice parameters a/a_0 and c/c_0, (b) normalized bond length d/d_0, and (c) total and partial density of states of Ti_2SnN.

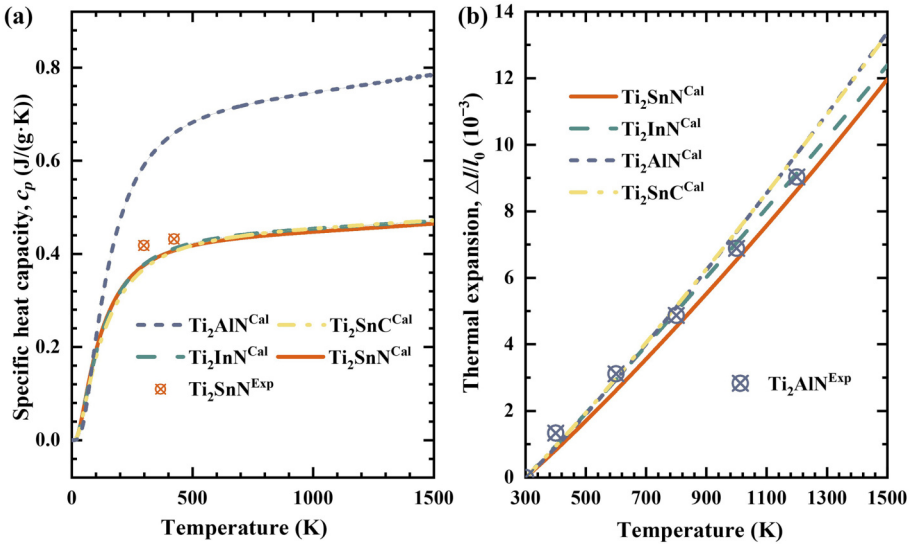

Fig. 9 (a) Calculated c_p (J·g^{-1}·K^{-1}) and (b) $\Delta l/l_0$ (10^{-3}) of Ti_2SnN, Ti_2AlN, Ti_2InN, and Ti_2SnC, while experimental thermal expansion data of Ti_2AlN [78] are also plotted for comparison.

((−3)–3 eV) appear in a higher energy range than the Ti–N bond (from −7 to −4 eV), indicating that the former is weaker, which is consistent with the bond stiffness theory and other typical MAXs [82].

The theoretically estimated specific heat capacity (c_p) using the QHA, including the contributions of phonons and electronic excitations of the four phases, is shown in Fig. 9(a). Notably, the predicted c_p of Ti_2AlN matches well with other calculation results [83]. c_p can be fitted via Eq. (22) [84]:

$$c_p = A_{c_p} + 10^{-6} B_{c_p} T - \frac{10^3 C_{c_p}}{T^2} \quad (22)$$

where T is the temperature (K); A_{c_p} (J·g^{-1}·K^{-1}), B_{c_p} (J·g^{-1}·K^{-2}), and C_{c_p} (J·K·g^{-1}) are the fitting parameters (Eq. (22)) for these MAX phases (300–1500 K). Like S-containing MAX phases [47], the parameter that most affects the specific heat capacity (A_{c_p}) is governed entirely by the average relative atomic mass u, defined as the molar mass divided by the atomic number, with the equation A_{c_p} = 23.97/u. Moreover, B_{c_p} and C_{c_p} exhibit minor shifts within the ranges of [0, 100] J·g^{-1}·K^{-2} and [0, 20] J·K·g^{-1}, respectively, at different temperatures. Therefore, it is not difficult to expect that the specific heat capacity of Ti_2SnN (u = 57.1125) is basically the same as that of Ti_2InN (u = 56.1375) and Ti_2SnC (u = 56.6125). The experimental specific heat capacities of Ti_2SnN at room temperature and 150 °C are 0.418 and 0.431 J·g^{-1}·K^{-1}, respectively. The corresponding differences between the experimental and calculated values at these temperatures are +11% (0.375 J·g^{-1}·K^{-1}) and +6% (0.407 J·g^{-1}·K^{-1}), demonstrating the accuracy of the calculations.

The estimated $\Delta l/l_0$ with the contribution of electronic excitations at 300–1500 K is shown in Fig. 9(b), including the experimental data of Ti_2AlN [78] for comparison. By fitting by the function $\Delta l/l_0 = \alpha \cdot (T - 300)$ from 300 to 1500 K, α is listed in Table 3. In all the cases, the calculated values were generally slightly greater than the experimental values, with the peak difference being less than 10%, because the GGA functional used overestimates the cell volume (Table 2), resulting in a lower bond strength in the simulations. Although the α of Ti_2SnN (10.06×10^{-6} K^{-1}) is indeed greater than that of the other phases, it is indeed greater than that of most MAX phases, such as Ti_2AlC (8.1×10^{-6} K^{-1}), Ti_3SiC_2 (α = 9.3×10^{-6} K^{-1}), and Ti_3AlC_2 (9.2×10^{-6} K^{-1}), and only smaller than a small number of phases, such as Cr_2GeC (14.5×10^{-6} K^{-1}), Cr_2AlC (12.6×10^{-6} K^{-1}), and Ti_2AlN ($\alpha = 10\times10^{-6}$ K^{-1}) [9].

4 Summary and conclusions

A composition-stability ML model was established for the MAX phases from the data of existing experimental and computational stability as well as atomic properties, where all the predicted stable phases were validated via a first-principles approach. Furthermore, one of the predicted MAX phases, Ti_2SnN, was experimentally synthesized, confirming the reliability of this ML model. In addition, the mechanical and thermal properties of Ti_2SnN were also briefly predicted. The main conclusions are as follows:

1) Using the ML model trained on existing experimental and computational data with the random forest classifier, support vector machine, and gradient boosting tree algorithms, the stability of 4347 MAX phases was quickly examined. Among them, 198 MAX phases were screened, 150 of which passed the criteria for thermodynamic stability and intrinsic stability. This approach avoids potential problems with incomplete thermodynamic competition phases and significantly enhances screening efficiency.

2) The factors that primarily influence the formation of MAX phases are $\overline{VEC}$ and S_{VEC}. $\overline{VEC}$ of a stable phase typically falls between 3.25 and 5, and it is located within three distinct, triangular-like regions, each with a width of 0.75 ($\overline{VEC}$) and a height of 0.3 (S_{VEC}). As $\overline{VEC}$ deviates further from integer values, the region of S_{VEC} capable of supporting stable phase formation gradually diminishes to the point where a $\overline{VEC}$ difference of 0.75 no longer allows for the formation of a stable phase.

3) The ML approach provides significant guidance for experimental efforts by narrowing promising candidates, thereby accelerating the discovery of new MAX phases. Here, the predicted stable Ti_2SnN was successfully synthesized under Ar protection at 750 °C for 5 h using Ti_2AlN and $SnCl_2$ in a 1 : 1.5 molar ratio, with its existence through XRD, Raman, SEM, and TEM and lattice parameters of a = 3.12468 Å, c = 13.6324 Å, and z_{Ti} = 0.0789. Interestingly, Ti_2SnN exhibits A-site element deintercalation and self-extrusion. On the basis of DFT calculations, Ti_2SnN exhibits a relatively low elastic modulus (B = 133 GPa, G = 78 GPa, and E = 196 GPa), high damage tolerance,

and high fracture toughness on the basis of the calculated ratio of the bond stiffness of the weakest and strongest bonds (k_{min}/k_{max} = 0.422). Its specific heat capacity is similar to that of Ti_2SnC, with a high α (10.06×10^{-6} K^{-1}). The synthesis and property analysis of Ti_2SnN highlight the tunability of MAX phases. With the discovery of Ti_2SnN, we have more options to select appropriate MAX phases for different applications.

Acknowledgements

This work was supported by the National Natural Science Foundation of China (No. 51972080).

Availability of data and materials

The data that support the findings of this study are available from the corresponding author upon reasonable request.

Competing interests

The authors have no competing interests to declare that are relevant to the content of this article. The author Yuelei Bai is the Editorial Committee member of this journal.

Electronic Supplementary Material

Supplementary material is available in the online version of this article at https://doi.org/10.26599/JAC.2025.9221050.

References

[1] Bai YL, Qi XX, Duff A, *et al.* Density functional theory insights into ternary layered boride MoAlB. *Acta Mater* 2017, **132**: 69–81.
[2] Du YQ, Wang FL, Hu MH, *et al.* Stability and wettability of ternary carbide Mo_2Ga_2C in molten metals. *Ceram Int* 2023, **49**: 21449–21454.
[3] Ding HM, Li M, Li YB, *et al.* Progress in structural tailoring and properties of ternary layered ceramics. *J Inorg Mater* 2023, **38**: 845.
[4] Lei X, Lin NM. Structure and synthesis of MAX phase materials: A brief review. *Crit Rev Solid State* 2022, **47**: 736–771.
[5] Sun ZM. Progress in research and development on MAX phases: A family of layered ternary compounds. *Int Mater Rev* 2011, **56**: 143–166.
[6] Pan Y. W_2AlC: A new layered MAX phase to adjust the balance between strength and ductility. *Mater Today Chem* 2024, **35**: 101915.
[7] Rougab M, Gueddouh A. A DFT exploration of the stabilities, physical properties, and tensile strength of new synthesized Nb_2AC (A = Ni and Co) MAX phases. *Solid State Sci* 2024, **158**: 107733.
[8] Rougab M, Gueddouh A. Investigation of the stability and physical properties of the newly synthesized Ta_2AC (A = Co and Ni) MAX phases from first principles. *Solid State Sci* 2024, **154**: 107603.
[9] Barsoum M W. *MAX Phases: Properties of Machinable Ternary Carbides and Nitrides*. Weinheim (Germany): Wiley-VCH, 2013.
[10] Gonzalez-Julian J, Go T, Mack DE, *et al.* Thermal cycling testing of TBCs on Cr_2AlC MAX phase substrates. *Surf Coat Technol* 2018, **340**: 17–24.
[11] Greco G, Iucolano F, Roccaforte F. Ohmic contacts to gallium nitride materials. *Appl Surf Sci* 2016, **383**: 324–345.
[12] Fashandi H, Andersson M, Eriksson J, *et al.* Single-step synthesis process of Ti_3SiC_2 ohmic contacts on 4H-SiC by sputter-deposition of Ti. *Scripta Mater* 2015, **99**: 53–56.
[13] Borysiewicz MA, Kamińska E, Piotrowska A, *et al.* Ti–Al–N MAX phase, a candidate for ohmic contacts to n-GaN. *Acta Phys Pol A* 2008, **114**: 1061–1066.
[14] Zhou XB, Han YH, Shen XF, *et al.* Fast joining SiC ceramics with Ti_3SiC_2 tape film by electric field-assisted sintering technology. *J Nucl Mater* 2015, **466**: 322–327.
[15] Fitriani P, Septiadi A, Hyuk JD, *et al.* Joining of SiC monoliths using a thin MAX phase tape and the elimination of joining layer by solid-state diffusion. *J Eur Ceram Soc* 2018, **38**: 3433–3440.
[16] Tatarko P, Casalegno V, Hu CF, *et al.* Joining of CVD-SiC coated and uncoated fibre reinforced ceramic matrix composites with pre-sintered Ti_3SiC_2 MAX phase using spark plasma sintering. *J Eur Ceram Soc* 2016, **36**: 3957–3967.
[17] Pan Y, Xu LR. New insight into the structural, mechanical and thermodynamic properties of Mo_2C MXene as the ultrahigh temperature ceramics. *Mater Today Chem* 2024, **42**: 102449.
[18] Zhang Y, Wang L, Zhang N, *et al.* Adsorptive environmental applications of MXene nanomaterials: A review. *RSC Adv* 2018, **8**: 19895–19905.
[19] Unal MA, Bayrakdar F, Fusco L, *et al.* 2D MXenes with antiviral and immunomodulatory properties: A pilot study against SARS-CoV-2. *Nano Today* 2021, **38**: 101136.
[20] Kang ZM, Khan MA, Gong YM, *et al.* Recent progress of MXenes and MXene-based nanomaterials for the electrocatalytic hydrogen evolution reaction. *J Mater Chem A* 2021, **9**: 6089–6108.
[21] Rackl T, Eisenburger L, Niklaus R, *et al.* Syntheses and physical properties of the MAX phase boride Nb_2SB and the solid solutions $Nb_2SB_xC_{1-x}$ (x = 0–1). *Phys Rev Materials* 2019, **3**: 054001.
[22] Zhang QQ, Zhou YC, San XY, *et al.* Zr_2SeB and Hf_2SeB: Two new MAB phase compounds with the Cr_2AlC-type MAX phase (211 phase) crystal structures. *J Adv Ceram* 2022, **11**: 1764–1776.
[23] Ingason AS, Petruhins A, Dahlqvist M, *et al.* A nanolaminated magnetic phase: Mn_2GaC. *Mater Res Lett,* 2014, **2**: 89–93.
[24] Dahlqvist M, Barsoum MW, Rosen J. MAX phases—Past, present, and future. *Mater Today* 2024, **72**: 1–24.
[25] Dahlqvist M, Alling B, Rosén J. Stability trends of MAX phases from first principles. *Phys Rev B* 2010, **81**: 220102.
[26] Qi XX, He XD, Yin WL, *et al.* Stability trend, weak bonding, and magnetic properties of the Al- and Si-containing ternary-layered borides MAB phases. *J Am Ceram Soc* 2023, **106**: 1513–1530.
[27] Ni N, Zhang HC, Zhou YC. Electronic structure, bonding characteristics, and mechanical behaviors of a new family of Si-containing damage-tolerant MAB phases M_5SiB_2 (M = IVB–VIB transition metals). *J Adv Ceram* 2022, **11**: 1626–1640.
[28] Ding H, Li Y, Li M, *et al.* Chemical scissor-mediated structural editing of layered transition metal carbides. *Science* 2023, **379**: 1130–1135.
[29] Shehab M, Abualigah L, Shambour Q, *et al.* Machine learning in medical applications: A review of state-of-the-art methods. *Comput Biol Med* 2022, **145**: 105458.
[30] Zhang J, Xu B, Xiong YX, *et al.* Design high-entropy carbide ceramics from machine learning. *NPJ Comput Mater* 2022, **8**: 5.
[31] Zhang L, He M, Shao SF. Machine learning for halide perovskite materials. *Nano Energy* 2020, **78**: 105380.
[32] Fan Y, Bai YL, Li Q, *et al.* Compositional design and phase formation capability of high-entropy rare-earth disilicates from machine learning and decision fusion. *NPJ Comput Mater* 2024, **10**: 95.
[33] Park H, Mall R, Alharbi FH, *et al.* Learn-and-match molecular cations for perovskites. *J Phys Chem A* 2019, **123**: 7323–7334.
[34] Schleder GR, Acosta CM, Fazzio A. Exploring two-dimensional materials thermodynamic stability via machine learning. *ACS Appl Mater Inter* 2020, **12**: 20149–20157.
[35] Fan Y, Bai YL, Lu ZY, *et al.* Exploring high-performance environmental barrier coatings for rare earth silicates: A combined approach of first principles calculations and machine learning. *J Materiomics* 2025, **11**: 100921.
[36] Frey NC, Wang J, Vega Bellido GI, *et al.* Prediction of synthesis of 2D metal carbides and nitrides (MXenes) and their precursors with positive and unlabeled machine learning. *ACS Nano* 2019, **13**: 3031–3041.
[37] Xu X, Zhang X, Bitzek E, *et al.* Origin of the yield stress anomaly in $L1_2$ intermetallics unveiled with physically informed machine-learning potentials. *Acta Mater* 2024, **281**: 120423.
[38] Liu YC, Chu KL, Zhou Y, *et al.* Discovery of orthorhombic perovskite oxides with low thermal conductivity by first-principles calculations. *J Adv Ceram* 2022, **11**: 1596–1603.
[39] Islam N, Huang WJ, Zhuang HL. Machine learning for phase

selection in multi-principal element alloys. *Comp Mater Sci* 2018, **150**: 230–235.
[40] Zhou ZQ, Zhou YJ, He QF, *et al.* Machine learning guided appraisal and exploration of phase design for high entropy alloys. *npj Comput Mater* 2019, **5**: 128.
[41] Kaufmann K, Vecchio KS. Searching for high entropy alloys: A machine learning approach. *Acta Mater* 2020, **198**: 178–222.
[42] Zhang L, Chen HM, Tao XM, *et al.* Machine learning reveals the importance of the formation enthalpy and atom-size difference in forming phases of high entropy alloys. *Mater Design* 2020, **193**: 108835.
[43] Zhang Y, Wen C, Wang CX, *et al.* Phase prediction in high entropy alloys with a rational selection of materials descriptors and machine learning models. *Acta Mater* 2020, **185**: 528–539.
[44] He M, Zhang L. Machine learning and symbolic regression investigation on stability of MXene materials. *Comp Mater Sci* 2021, **196**: 110578.
[45] Zhang Y, Xu W, Liu G, *et al.* Bandgap prediction of two-dimensional materials using machine learning. *PLOS One* 2021, **16**: 0255637.
[46] Zhang YM, Mao ZY, Han Q, *et al.* The role of Hume–Rothery's rules play in the MAX phases formability. *Materialia* 2020, **12**: 100810.
[47] Lu ZY, He XD, Yin H, *et al.* Theoretical screening, intrinsic brittleness and thermal properties of the S-containing MAX carbides and borides. *J Materiomics* 2023, **9**: 1056–1066.
[48] Malik AM, Rohrer J, Albe K. Theoretical study of thermodynamic and magnetic properties of transition metal carbide and nitride MAX phases. *Phys Rev Materials* 2023, **7**: 044408.
[49] Jeitschko W, Nowotny H, Benesovsky F. Die H-phasen Ti_2TlC, Ti_2PbC, Nb_2InC, Nb_2SnC und Ta_2GaC. *Monatsh Chem Verw Tl* 1964, **95**: 431–435.
[50] Zhang YM, Xu YJ, Huang Q, *et al.* Structure maps for MAX phases formability revisited. *Ceram Int* 2024, **50**: 2855–2863.
[51] Eklund P, Beckers M, Jansson U, *et al.* The $M_{n+1}AX_n$ phases: Materials science and thin-film processing. *Thin Solid Films* 2010, **518**: 1851–1878.
[52] Barsoum MW, Farber L. Room-temperature deintercalation and self-extrusion of Ga from Cr_2GaN. *Science* 1999, **284**: 937–939.
[53] Cordero B, Gómez V, Platero-Prats AE, *et al.* Covalent radii revisited. *Dalton T* 2008: 2832.
[54] Oyedele O. Determining the optimal number of folds to use in a K-fold cross-validation: A neural network classification experiment. *Res Math* 2023, **10**: 2201015.
[55] Kresse G, Furthmüller J. Efficient iterative schemes for *ab initio* total-energy calculations using a plane-wave basis set. *Phys Rev B* 1996, **54**: 11169–11186.
[56] Perdew JP, Burke K, Ernzerhof M. Generalized gradient approximation made simple. *Phys Rev Lett* 1996, **77**: 3865–3868.
[57] Popoola AI, Oluyamo SS. Physical properties of some noble metal compounds from PAW-DFT calculations. *J Sci Technol* 2015, **34**: 47.
[58] Togo A, Tanaka I. First principles phonon calculations in materials science. *Scripta Mater* 2015, **108**: 1–5.
[59] Kroumova E, Aroyo MI, Perez-Mato JM, *et al.* Bilbao crystallographic server: Useful databases and tools for phase-transition studies. *Phase Transit* 2003, **76**: 155–170.
[60] Hill R. The elastic behaviour of a crystalline aggregate. *P Phys Soc Lond A* 1952, **65**: 349–354.
[61] Bai YL, He XD, Wang RG, *et al.* An *ab initio* study on compressibility of Al-containing MAX-phase carbides. *J Appl Phys* 2013, **114**: 173709.
[62] Bai YL, Qi XX, He XD, *et al.* Phase stability and weak metallic bonding within ternary-layered borides CrAlB, Cr_2AlB_2, Cr_3AlB_4, and Cr_4AlB_6. *J Am Ceram Soc* 2019, **102**: 3715–3727.
[63] Kashiwaya S, Lai CC, Lu J, *et al.* Formation of Ti_2AuN from Au-covered Ti_2AlN thin films: A general strategy to thermally induce intercalation of noble metals into MAX phases. *Cryst Growth Des* 2020, **20**: 4077–4081.
[64] Presser V, Naguib M, Chaput L, *et al.* First-order Raman scattering of the MAX phases: Ti_2AlN, $Ti_2AlC_{0.5}N_{0.5}$, Ti_2AlC, $(Ti_{0.5}V_{0.5})_2AlC$, V_2AlC, Ti_3AlC_2, and Ti_3GeC_2. *J Raman Spectrosc* 2012, **43**: 168–172.
[65] Raghavan V. Al–N–Ti (aluminum–nitrogen–titanium). *J Phase Equilib Diff* 2006, **27**: 159–162.
[66] Jeitschko W, Nowotny H, Benesovsky F. Die H-phasen: Ti_2CdC, Ti_2GaC, Ti_2GaN, Ti_2InN, Zr_2InN und Nb_2GaC. *Monatsh Chem Verw Tl* 1964, **95**: 178–179.
[67] Manoun B, Leaffer OD, Gupta S, *et al.* On the compression behavior of Ti_2InC, $(Ti_{0.5},Zr_{0.5})_2InC$, and M_2SnC (M = Ti, Nb, Hf) to quasi-hydrostatic pressures up to 50 GPa. *Solid State Commun* 2009, **149**: 1978–1983.
[68] Liu Y, Zhang P, Ling C, *et al.* Spontaneous Sn whisker formation on Ti_2SnC. *J Mater Sci Mater El* 2017, **28**: 5788–5795.
[69] Li M, Lu J, Luo K, *et al.* Element replacement approach by reaction with lewis acidic molten salts to synthesize nanolaminated MAX phases and MXenes. *J Am Chem Soc* 2019, **141**: 4730–4737.
[70] Sun ZM, Hashimoto H, Tian WB, *et al.* Synthesis of the MAX phases by pulse discharge sintering. *Int J Appl Ceram Tec* 2010, **7**: 704–718.
[71] Roy C, Banerjee P, Bhattacharyya S. Molten salt shielded synthesis (MS^3) of Ti_2AlN and V_2AlC MAX phase powders in open air. *J Eur Ceram Soc* 2020, **40**: 923–929.
[72] Khediri R, Hammoutène D, Kassali K, *et al.* High-pressure structural, elastic, vibrational, and thermodynamic study of MAX-phase Ti_2InN. *Comput Condens Matter* 2023, **36**: 00829.
[73] Manoun B, Zhang FX, Saxena SK, *et al.* X-ray high-pressure study of Ti_2AlN and Ti_2AlC. *J Phys Chem Solids* 2006, **67**: 2091–2094.
[74] Bentzel GW, Naguib M, Lane NJ, *et al.* High-temperature neutron diffraction, Raman spectroscopy, and first-principles calculations of Ti_3SnC_2 and Ti_2SnC. *J Am Ceram Soc* 2016, **99**: 2233–2242.
[75] Lin ZJ, Zhuo MJ, Li MS, *et al.* Synthesis and microstructure of layered-ternary Ti_2AlN ceramic. *Scripta Mater* 2007, **56**: 1115–1118.
[76] Lapauw T, Vanmeensel K, Lambrinou K, *et al.* Rapid synthesis and elastic properties of fine-grained Ti_2SnC produced by spark plasma sintering. *J Alloys Compd* 2015, **631**: 72–76.
[77] Cygan T, Wozniak J, Broniszewski K, *et al.* Analysis of microstructure and mechanical properties of alumina composites reinforced with Ti_2AlN MAX phases. *Int J Refract Met H* 2024, **122**: 106725.
[78] Lane NJ, Vogel SC, Barsoum MW. Temperature-dependent crystal structures of Ti_2AlN and Cr_2GeC as determined from high temperature neutron diffraction. *J Am Ceram Soc* 2011, **94**: 3473–3479.
[79] Murnaghan FD. The compressibility of media under extreme pressures. *P Natl Acad Sci USA* 1944, **30**: 244–247.
[80] Zhou WB, Liu L, Zhu JQ, *et al.* Facile synthesis of high-purity Ti_2SC powders by spark plasma sintering technique. *Ceram Int* 2017, **43**: 9363–9368.
[81] He XD, Bai YL, Zhu CC, *et al.* Polymorphism of newly discovered Ti_4GaC_3: A first-principles study. *Acta Mater* 2011, **59**: 5523–5533.
[82] Bai YL, He XD, Wang RG. Lattice dynamics of Al-containing MAX-phase carbides: A first-principle study. *J Raman Spectrosc* 2015, **46**: 784–794.
[83] Djedid A, Méçabih S, Abbes O, *et al.* Theoretical investigations of structural, electronic and thermal properties of Ti_2AlX (X = C, N). *Physica B* 2009, **404**: 3475–3482.
[84] Qi XX, Yin WL, Jin S, *et al.* Density-functional-theory predictions of mechanical behaviour and thermal properties as well as experimental hardness of the Ga-bilayer Mo_2Ga_2C. *J Adv Ceram* 2022, **11**: 273–282.